Article

Microstructural Insights into the Transformation of Cubic, Low-Temperature, Disordered Cu$_2$ZnSnS$_4$ into the Tetragonal Form

S. Bette,* E. Isotta,* B. Mukherjee,* A. Schulz, Z. Dallos, U. Kolb, Robert E. Dinnebier, and P. Scardi

Read Online

ACCESS | Metrics & More | Article Recommendations | Supporting Information

ABSTRACT: Multinary earth-abundant chalcogenides, like kesterite, Cu$_2$ZnSnS$_4$ (CZTS), have attracted attention in sustainable energy applications like photovoltaics and thermoelectrics. High-energy ball milling provides a facile way for the synthesis of pure cubic CZTS. This sulfide crystallizes in a sphalerite-type structure with complete occupational disorder in the cationic substructure and a considerable amount of stacking faults. Heating of the material leads to the slow and irreversible transition into disordered, tetragonal kesterite, which is associated with a significant decrease in thermoelectric properties. Hence, a deep understanding of the phase transition process and its kinetics is a prerequisite for further crystal engineering. *In situ* X-ray powder

diffraction and Raman spectroscopy supported by density functional theory calculations and *ab initio* molecular dynamics simulations (AIMD) were employed to gain microstructural insights into the phase transition process. Heating leads to a growth of the crystalline domains, which is associated with a reduction of strain. The domain growth reduces the stabilization of the metastable cubic phase by nanostructuring. This eventually leads to the segregation of tin cations, which corresponds to the beginning of the transition into the tetragonal phase. AIMD simulations indicate that the presence of faulting planes promotes the tin diffusion. As stacking faults appear to be energetically less favorable in the tetragonal disordered form, the stacking fault disorder is reduced upon heating, leading to an additional strain reduction.
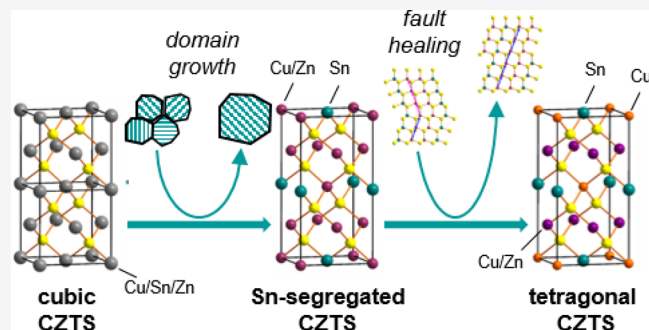
INTRODUCTION

Cu$_2$ZnSn(S,Se)$_4$ (CZTS and CZTSe) materials, belonging to the class of quaternary diamond-like semiconductors, have recently attracted attention in various fields of energy materials. Owing to the structural similarity with Cu(InGa)Se$_2$, they have been proposed as possible alternatives for thin-film photovoltaic applications, deemed promising for their compositional abundance, optimal bandgap value, and high absorption coefficient.[1,2] They have also been investigated as thermoelectric materials,[3−5] exhibiting interesting conversion performance when the carrier density is optimized.[6−9] At room temperature, CZTS and CZTSe are characterized by the tetragonal $I\bar{4}$ kesterite structure, from which they sometimes take the name.[10] This structure is closely related to the zincblende or sphalerite type and thus consists of a tetrahedral coordination of S (or Se) anions and a corresponding ordered motif of cations. These arrange into two alternating Cu−Zn and Cu−Sn layers. Given the structural complexity and multinary nature, cation antisites and lattice defects are quite common. Among those with the lowest formation energy are Cu$_{Zn}$ and Cu$_{Sn}$ antisites and Cu vacancies,[11] all behaving as acceptors and thus deemed responsible for the p-type nature of these compounds.[12] At relatively low temperatures, namely, 533 K for CZTS[13] and 473 K[14] for CZTSe, the kesterite structure is reported to transition to the $I\bar{4}2m$ tetragonal

arrangement, sometimes referred to as disordered kesterite.[15] This differs from the $I\bar{4}$ kesterite as the cation occupancy in the Cu−Zn planes becomes completely randomized.[16] Given the energetic proximity of these two structures, sometimes, the $I\bar{4}2m$ is reported coexisting at room temperature with the $I\bar{4}$ one.[15] These order−disorder transitions, second-order and reversible, have been shown to cause a significant impact on materials properties. From a photovoltaic perspective, Cu−Zn disorder was associated with trap states that increase carrier recombination.[14,17] This triggered several studies to assess the impact on the overall performance,[13,18,19] with the current understanding pointing to extensive disorder and Sn$_{Zn}$ antisites as the origin of photovoltaic performance loss.[20] In thermoelectric CZTS, it was recently shown that the Cu−Zn order−disorder transition leads to a sharp increase in the Seebeck coefficient.[21,22] This originates from a modification to the band structure featuring heavier mass and more converged bands.[23]
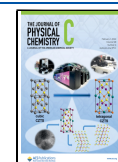
In tetragonal CZTSe, instead, the transition leads to a decrease in electrical resistivity,[7] mainly attributed to the bandgap reduction.[24]

Other polymorphs have been reported in the literature for the same compositions.[25] When synthesized through high-energy mechanical alloying, CZTS and CZTSe were shown to arrange in a cubic sphalerite-like $F\bar{4}3m$ structure, with full Cu−Zn−Sn disorder on the cation site.[24−27] This arrangement is metastable, transitioning to the tetragonal structure above ∼650 K.[25] Interestingly, disordered cubic polymorphs have been reported leading to superior thermoelectric performance. This was partially attributed to an ultralow thermal conductivity, arising from low phonon group velocities and low-lying optical modes.[24,28] Recently, the extensive cation disorder in cubic CZTS was shown to be responsible for a topologically nontrivial electronic structure.[29]

In addition to these arrangements, Lu et al.[30] along with several successive works[31,32] showed that, when synthesized with dodecanethiol, CZTS seems to form a hexagonal $P6_3mc$ structure derived from the ZnS wurtzite. This can also be seen as an extensive "faulting" in the standard stacking of tetragonal kesterite. This is not surprising as numerous reports evidenced that stacking faults are common in this compound,[25,33−36] and regions of tetragonal and hexagonal CZTS can coexist in a single sample.[37,38]

It results that the large variety of energetically shallow defects in CZTS fosters a marked polymorphism, and often phase coexistence. Different phases have been shown to markedly affect transport properties, with critical consequences on the photovoltaic and thermoelectric conversion efficiencies. As such, we believe that an accurate understanding of the temperature stability and evolution of the different phases, as well as of stacking faults, is important to aid the establishment of these materials for energy applications.

In this work, we present a careful investigation of the irreversible and slow transition process of stacking faulted, disordered cubic CZTS into disordered tetragonal CZTS supported by temperature-dependent *in situ* X-ray powder diffraction (XRPD) and Raman spectroscopy. The temperature-induced growth of the domains triggers the segregation of the tin cations within the cation substructure, i.e., the transition into the tetragonal phase. Subsequently, the degree of stacking fault disorder decreases. Large-scale density functional theory (DFT) calculations suggest that stacking faults are energetically less favorable in the tetragonal polymorph, and *ab initio* molecular dynamics (AIMD) simulations indicate that tin ordering is initiated in the presence of faulting planes. These findings point to stacking faults playing a significant role in the order−disorder phase transition of CZTS and having a major impact on the thermal stability of disordered, cubic kesterite. The irreversible phase transition from disordered cubic CZTS into the tetragonal polymorph leads to a tremendous reduction of the thermo-electric properties.[28] Hence, detailed knowledge on this transition is a prerequisite for further crystal engineering aiming to stabilize the cubic, disordered CZTS phase.

■ MATERIALS AND METHODS

Phase Synthesis. CZTS powders were synthesized via reactive mechanical alloying in a planetary mill (Fritsch P4 Pulverisette 4), adapting the procedure described elsewhere.[26] Elemental precursors (Cu powder, <75 μm, 99%; Zn powder, purum, 99%; Sn powder, puriss, 99%; S flakes, purum, 99.5%;

all by Sigma-Aldrich) were weighted in a stoichiometric quantity and loaded into an 80 mL WC vial in a glovebox (Ar-filled, O_2 partial pressure of <10 ppm) together with 27 12 mm-diameter tungsten carbide (WC) balls. A ball-to-powder weight ratio of 100:1 was used. The elemental powders were milled in high-energy conditions for 120 min with jar rotation speed ω = −601.4 rpm and main disk revolution speed Ω = 310 rpm, for a fixed ratio ω/Ω = −1.94. Some of the powders were then heat-treated at 300 °C for 20 min (with a heating rate of 20 K/min) in a static atmosphere of Ar to increase the crystallinity.

Phase Characterization. The XRPD patterns of the solid phases were collected on a laboratory powder diffractometer in Debye−Scherrer geometry (Stadi P-Diffractometer, Stoe), Ag $K_{\alpha 1}$ radiation from a primary Ge(111)-Johann-type mono-chromator, and a triple array of Mythen 1 K detectors (Dectris). The samples were sealed under an argon atmosphere in 0.3 mm-diameter quartz capillaries (Hilgenberg glass), which were spun during the measurement. Heating of the capillaries was performed with a gas blower (GSB 1300, FMB Oxford) applying a heating rate of 5 K/min. Temperature-dependent XRPD measurements were performed at room temperature and subsequently between 300 and 550 °C using 10 K steps, with a 5 min delay prior to the XRPD measurements for thermal equilibration and applying a scan time of 4 h. Isothermal XRPD measurements were performed by collecting XRPD data at room temperature and after subsequent heating to 350, 375, 400, and 500 °C. XRPD patterns were continuously recorded applying a scan time of 30 min.

Raman spectra were recorded using a Jobin Yvon Typ V 010 LabRAM single grating spectrometer, equipped with a double super razor edge filter and a Peltier-cooled charge-coupled device camera. The resolution of the spectrometer (grating, 1800 lines/mm) was 1 cm^{-1}. The spectra were taken in a quasi-backscattering geometry using the different linearly polarized laser with a wavelength of 633 nm. The power was lower than 1 mW, to protect against local heating. The spot size was 20 μm, focused by a 20× microscope objective onto the surface of the sample. For heating experiments, the setup was equipped with a heating microscope stage (THMS600, controlled by a Linkam TMS 94). The scanning range was from 25 to 600 °C at a ramping rate of 10 °C min^{-1} under a nitrogen atmosphere. Measurements were taken at temperatures ranging between 25 and 600 °C with a 1 °C accuracy.

TEM experiments were performed with a FEI Tecnai F30-ST working at a 300 keV acceleration voltage. The samples were prepared by drop casting an ultrasound-treated ethanol dispersion on a continuous carbon-coated Cu grid. For heating experiments, a Gatan single tilt heating holder was used.

The program TOPAS 6.0[39] was used to analyze the XRPD patterns. The background of the diffraction patterns was modeled by Chebychev polynomials of the sixth order and the peak profile by using the fundamental parameter approach implemented into TOPAS.[40,41] The instrumental resolution function had been determined by a Pawley fit[42] of a LaB$_6$ standard measurement prior to the experiments. A supercell approach implemented into TOPAS[43] averaging 100 supercells containing 500 layers each was used for modeling the stacking fault disorder of the samples using the microstructure model that we outlined in our previous study.[25] Multidimensional grid search routines[44,45] were employed to find the global minimum in the parameter space of the transition probabilities.
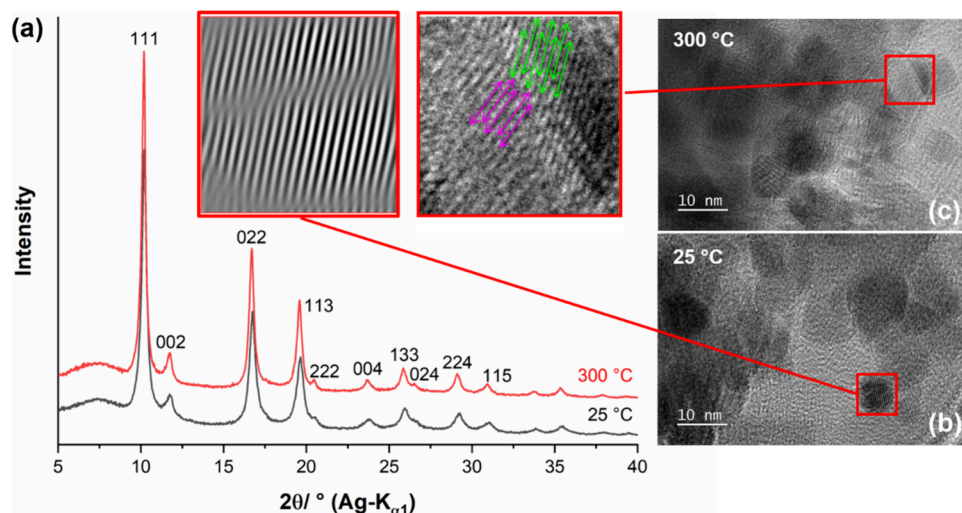
Figure 1. (a) XRPD patterns of cubic disordered CZTS recorded at 25 and 300 °C including selected reflection indices and TEM images taken at 25 (b) and 300 °C (c) highlighting structural disorder (25 °C: red box) and misaligned domains (300 °C: red box, magenta and green arrows).

Density Functional Theory (DFT) and *Ab Initio* Molecular Dynamics (AIMD). The faultless cubic and disordered tetragonal polymorphs of CZTS were modeled with 64 ion supercells, which were then repeated infinitely in each direction (periodic boundary conditions). The structure was based on a $2 \times 2 \times 2$ cubic sphalerite (ZnS) unit cell, with half the cation sites occupied by Cu ions and 1/4 each occupied by Zn and Sn ions. In the disordered tetragonal structure, the cations in the Cu/Zn layer were randomized, while the Cu/Sn layer remained ordered. For the cubic polymorph instead, all cation site occupancies were randomly assigned. The lowest energy configuration, as determined from a previous study,[29] was chosen from 10 such random structures, though it should be noted that the cohesive energies of the different configurations of disorder were only a few meV/ion apart and did not significantly affect the properties of the system. To simulate the faults in the disordered structures, larger, more complicated 256 ion supercells ($4 \times 4 \times 4$ sphalerite unit cells) were built up, which preserved both the stoichiometry and randomization of disordered CZTS, while introducing a stacking fault (Supporting Information, Figure S7). The large size of the supercells, for both faultless and faulted structures, provided a large number of cation sites (32 and 128, respectively), thus ensuring an appropriately randomized distribution of the cations.

The DFT calculations and AIMD simulations were performed using the Vienna *ab initio* simulation package (VASP).[46,47] The electron-exchange correlation functional was approximated using the Perdew–Burke–Ernzerhof (PBE)[48] form of the generalized gradient approximation, with the scalar-relativistic PBEsol pseudopotentials.[49] All calculations were performed with an energy cutoff of 450 eV and a Gaussian charge smearing of 0.1 eV. The Brillouin zone (BZ) for the 64 atom supercells was sampled with a $2 \times 2 \times 2$ k-mesh, while for the large 256 atom supercells, the BZ was sampled only at the gamma point. The geometry of the supercells was relaxed until the Hellmann–Feynman forces on individual ions were reduced to below 10^{-6} ev/Å. The *ab initio* molecular dynamics simulations were performed within a canonical (NVT) ensemble connected to a heat bath with a Nose–Hoover thermostat set to 300 and 600 K (below the

transition) and 750 K (above the transition) for multiple trajectories. For the 64 ion unit cells, the system was allowed to evolve with a time step of 2 fs, for 10,000 steps, corresponding to a total simulation time of 20 ps. For the 256-ion system, the number of time steps was reduced to 5000 due to the increased computational cost, with a simulation time of 10 ps. The atomic root-mean-square displacement (RMSD) was obtained from the MD trajectories, with the diffusion coefficient obtained from the slope of the RMSD.

RESULTS AND DISCUSSION

Phase Characterization. High-energy ball milling using copper, zinc, and tin metals, sulfur, and WC balls and jars leads to the formation of pure, cubic, disordered Cu_2ZnSnS_4. In the diffraction pattern, all observed reflections can be indexed to a cubic, sphalerite-like unit cell with $a = 5.435(1)$ Å (Figure 1, a, black line and indices). The broad shape of the peaks indicates a small domain size, while anisotropic broadening of the (002) and (022) reflections points to structural disorder in terms of stacking faults as discussed in our previous work.[25] Typically, after ball milling, a heat treatment at 300 °C is performed[25] in order to increase the crystallinity of the product. *In situ* XRPD confirms that the cubic, disordered form of CZTS is maintained at this temperature, and sharpening of the reflections points to a growth of the mean domain size (Figure 1a, red line). The small, rounded, and strongly aggregated characteristics of the CZTS particles after ball milling provide a serious obstacle for an in-depth TEM analysis (Figure 1b). The small particle size can be visualized as well as the presence of defects (Figure 1b, red framed inset). Atomistic images of stacking fault disorder, however, cannot be resolved. We performed the heat treatment process *in situ* in the TEM (Figure 1c). The particles seem to become slightly larger, and more details, like domains being misaligned (Figure 1c, red framed inset, green and magenta arrows), can be revealed.

Transformation of Disordered Cubic Cu_2ZnSnS_4 into the Tetragonal Form. The thermal stability of cubic, disordered CZTS is limited by the irreversible phase transition to the disordered tetragonal form, occurring at approximately 400 °C. Both disordered forms are structurally strongly related. In disordered, cubic CZTS crystallizing in the space group $F\bar{4}3m$, all cations are distributed statistically over the 4*c*
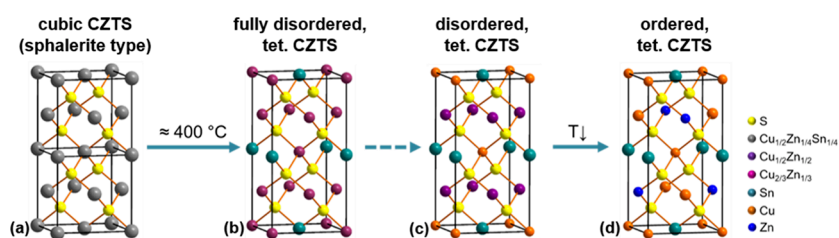
Figure 2. Atomistic picture of the temperature-induced transformation of disordered, cubic CZTS (a) into tetragonal disordered CZTS (c) via a potential fully disordered state (b).[51] Subsequent cooling leads to the formation of ordered tetragonal CZTS (d).
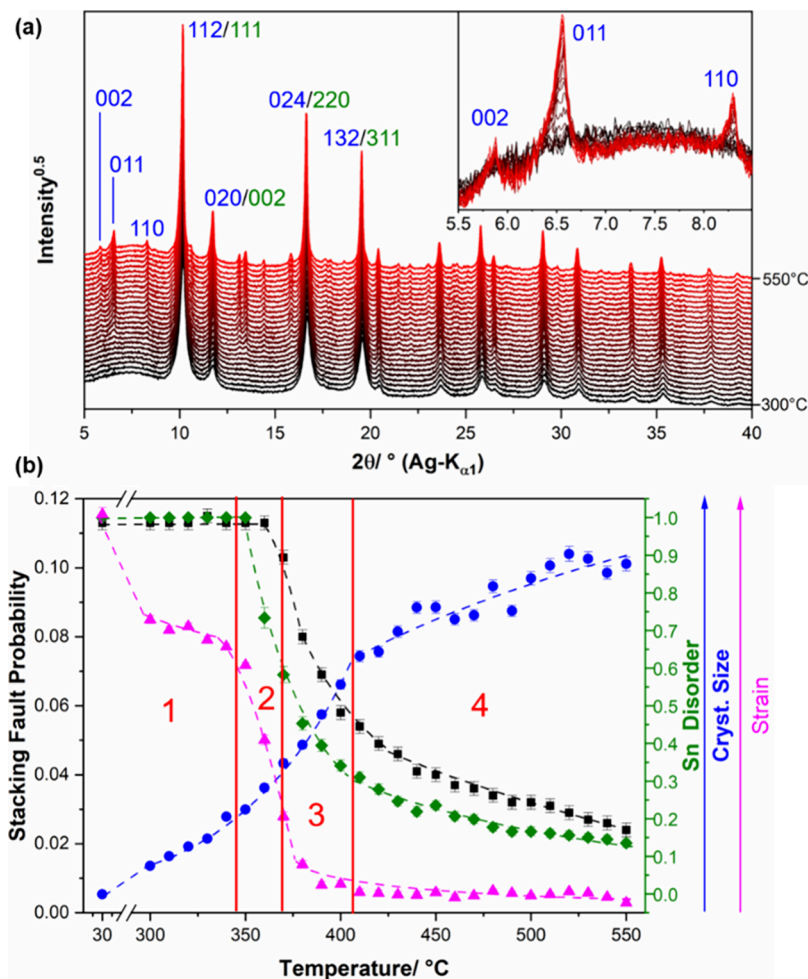

Figure 3. (a) *In situ* XRPD patterns recorded during the heating of CZTS including selected reflection indices for the cubic (green font color) and tetragonal cell (blue font color), (b) results of the XRPD analyses separating the transition process into four phases: (1) domain growth, (2) tin segregation, (3) fault healing, and (4) continuous state. The errors for Sn disorder, strain, and cryst. size are smaller than the symbol size.

position (Figure 2a, gray balls). The transition into the tetragonal, disordered polymorph leads to a doubling of the unit cell and to a reduction to $I\bar{4}2m$ space group symmetry.[15] Tin and copper cations are situated on planes perpendicular to the *c*-axis occupying 2*a* and 2*b* sites, respectively (Figure 2c, orange and petrol balls). In the cation substructure, these planes alternate with planes populated by occupationally disordered copper and zinc cations situated on a 4*d* site (Figure 2c, violet balls). Subsequent cooling leads to an ordering of zinc and copper cations, which is associated with a further reduction of the space group symmetry to $I\bar{4}$ (Figure 2d). It should be noted that this ordering is incomplete in many cases and depends on the cooling rate.[16,50] The transition from disordered cubic into disordered tetragonal

CZTS could be more complex: theoretical studies[51] point to the existence of an intermediary "fully disordered" tetragonal form, which could be described with $I\bar{4}2m$ space group symmetry, with ordered tin cations occupying the 2*b* site and occupationally disordered copper and zinc cations being statistically distributed over 2*a* and 4*d* sites (Figure 2b, light violet balls). Hence, the phase transition can be described by a segregation of tin cations that is followed by a partial segregation of copper and zinc cations. In our previous study,[25] we found that the stacking fault disorder, present in ball-milled, disordered, cubic, CZTS, disappears after the transition to the tetragonal polymorph. This and the slow and sluggish character of the phase transition indicate that the process is more complex than illustrated in Figure 2.

Temperature-Dependent *In Situ* XRPD Analyses. The *in situ* XRPD patterns of disordered cubic CZTS, recorded between 300 and 550 °C in 10 K intervals, are presented in Figure 3a. During heating, the reflections sharpen, which indicates both an increase in the domain size and a reduction of the microstrain. The changes in the peak profile, in particular in the profile of the (002) reflection (Figure 3a, green indices, and Supporting Information, Figure S1), also point to a reduction of the stacking fault disorder induced by heating. The most prominent change in the XRPD pattern upon heating is the appearance of supercell reflections (Figure 3a, blue indices), which can be indexed with the tetragonal cell of disordered, tetragonal kesterite.[15] As these reflections appear as sharp peaks and only grow in intensity, we assume that heating induces a slow segregation of the tin cations within the crystal lattice, leading to an incremental transformation from cubic to disordered, tetragonal CZTS.

In order to gain more detailed insight into this phase transition, we performed fully weighted Rietveld-based[52] analyses of the XRPD patterns including quantification of the microstrain (Figure 3b, magenta triangles), domain size (blue circles) parameters, degree of stacking fault disorder (black squares), and degree of tin disorder (green diamonds). Some examples of the graphical results of the refinements are presented in the Supporting Information in Figure S2. As the deconvolution of strain and domain size parameters from the peak profile is not trivial and some parameter correlation cannot be avoided, we will interpret trends rather than absolute values. As such, absolute scales for domain size and microstrain are omitted in Figure 3. It must also be noted that the domain size parameter is only a rough approximation as it does not take bi- or multimodal domain size distributions into account and does not correct for anisotropic particle shapes. That is why we adopt the simplification, i.e., a scalar representation, reducing the domain size and microstrain effects to a single number. In addition, more sophisticated approaches that implement these features for domain size broadening effects, like whole powder pattern modeling (WPPM),[53,54] are not yet compatible with the routines that include stacking faults into the refinements. In general, the amount of details and information that can be extracted from the patterns is limited, which does not allow for the adoption of more sophisticated line profile models, such as those provided by a WPPM approach. The ordering of the tin cations was modeled by a parameter increasing the tin occupancy in 1/4 of the cation positions in any layer and decreasing the tin occupancy accordingly in the other 3/4 of the cation positions (Supporting Information, Figure S3 and Table S1). Heating of ball-milled CZTS initially leads to a growth of the domain size (Figure 3b1, blue circles), which is associated with a reduction of the short-range strain (magenta triangles), whereas both the stacking fault probability (black squares) and the tin disorder (green diamonds) remain constant below 350 °C. At temperatures above 350 °C, the tin disorder starts to decrease (Figure 3b2), and by further heating, the stacking fault disorder is reduced (3). The reduction of both the tin and the stacking fault disorder leads to a steep decrease in the long-range microstrain. At higher temperatures, above 410 °C (Figure 3b4), the system slowly transitions toward a stationary state, with the domain size growing only moderately (blue circles), both the decrease in tin (green diamonds) and stacking fault disorder (black squares) decelerating, and the microstrain reaching a plateau. In order to deepen the insight

into the transition mechanism, we performed isothermal experiments where as-milled CZTS samples were held at 350, 375, 400, and 500 °C (Supporting Information, Figure S4a−d) for 17 to 22 h. In the variable-temperature *in situ* XRPD measurements at 350 °C, only the growth of the domains and the reduction of the short-range strain could be seen (Figure 3b). Holding CZTS at 350 °C leads to a constant growth of the domain size and a reduction of the short-range microstrain (Supporting Information, Figure S4a). After 15 h, however, the tin disorder parameter (green diamonds) starts to drop down, which leads to a starting decrease in the stacking fault probability (black squares). The same effects can be seen in the data collected at 375 and 400 °C (Supporting Information, Figure S4b,c). After an initial increase, the domain size reaches a plateau, for 375 °C after 4 h, and for 400 °C after 2 h. Then, the tin disorder parameter exhibits a steep decrease followed by a much slower decrease in the stacking fault probability. At 500 °C, the transition occurs very quickly (Supporting Information, Figure S4d): after 2 h, the microstrain and the disorder parameters have already plateaued out, whereas the growth of the domain size continues for another 6 h. Based on these observations, we deduce the following mechanism for the transition from cubic, disorder CZTS into tetragonal CZTS: (i) increasing the temperature leads to a growth of the domains, most likely by coalescence of misaligned neighboring domains (Figure 1c), which reduces the strain; (ii) the domain growth leads to a loss of nanostructuration, which most likely destabilizes the meta-stable cubic CZTS. As a consequence, tin cations start to order within the crystal, which initiates the transition from cubic, disordered to tetragonal CZTS. (iii) The movement of the tin cations triggers a healing of the stacking faults leading to an additional microstrain reduction. Due to the quasi-identical atom form factors of copper and zinc, we cannot distinguish via XRPD whether the transition initially yields fully disordered tetragonal or disordered tetragonal kesterite (Figure 2).

Temperature-Dependent *In Situ* Raman Spectroscopy. In order to support the in-depth XRPD analyses, we recorded temperature-dependent *in situ* Raman spectra. For creating our own reference data for disordered cubic, disordered tetragonal, and ordered tetragonal CZTS, we heated up one sample multiple times: in the first heating cycle, the material was heated up to 400 °C with subsequent cooling to room temperature, and in the second and third heating cycle, the sample was heated up to 600 °C (Supporting Information, Figure S5). The Raman spectrum collected after the second heating cycle matches the reported data on ordered, tetragonal kesterite[55] (Figure 4, green line); hence, we assign the identical Raman spectra collected at 400 °C during the second and third run to disordered, tetragonal kesterite. The Raman spectrum of ordered, tetragonal kesterite (Figure 4, green line) can be clearly distinguished from the Raman spectra of the disordered polymorphs (blue and black lines). The spectrum of ordered, tetragonal kesterite exhibits sharp bands at 368, 338, 288, and 99 cm⁻¹, as well as a broad band at 74 cm⁻¹. The disordered form only exhibits broad, shoulder like bands at 367 and 295 cm⁻¹ for the cubic phase and at 363 and 290 cm⁻¹ for the tetragonal phase. Both phases show an intense but also broad main band at 329 (cubic, black line) and 332 cm⁻¹ (tetragonal, blue line), whereas the main band of the disordered tetragonal phase is clearly sharper. In disordered cubic CZTS measured before heating (black line), overtone bands located at around 675 and 1000 cm⁻¹ are absent, which
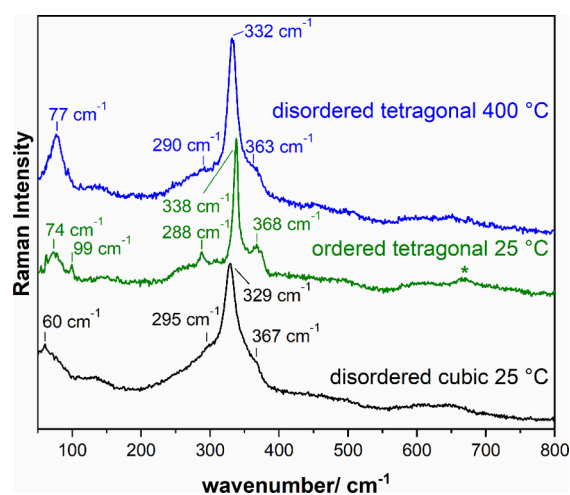
Figure 4. Raman spectra of disordered cubic CZTS (black line) and ordered tetragonal CZTS (green line), obtained by calcination of disordered cubic CZTS at 600 °C, both measured at 25 °C and Raman spectrum of the same sample measured at 400 °C after three heating cycles (Supporting Information, Figure S6), corresponding to disordered tetragonal CZTS (blue line), including positions of selected bands. The asterisk marks a small band, which is a potential overtone of the main band at 330−340 cm^{-1} appearing in the pattern of ordered tetragonal CZTS.

illustrates the poor crystallinity[56] of the sample obtained from reactive ball milling. In ordered tetragonal CZTS (green line), a broad feature located at around 675 cm^{-1} (Figure 4, green line, asterisk) could be considered as a weak overtone indicative of an increase in crystallinity, which goes along with the sharpening of the XRPD reflections and the growth in mean domain size that we observed (Figure 3a,b). Due to the limited resolution of an *in situ* Raman setup and the widths of these main bands, it is unreasonable to use the slight shift in the band position for monitoring the transition from the disordered cubic phase to the disordered tetragonal phase. There is, however, a difference in the spectra of both phases, which could be used for tracking the phase transition: the disordered cubic phase shows a broad band at 60 cm^{-1}, whereas the disordered tetragonal phase exhibits a somewhat sharper band at 77 cm^{-1}.

In the next step, we performed an isothermal heating experiment analogous to the isothermal XRPD measurements. Starting at 25 °C, the same sample was heated in 100 K steps, and Raman data were collected until it reached 400 °C, after 50 min (Figure 5a, green line). We observed the occurrence of the band located at 77 cm^{-1}, indicating the beginning of the transition from disordered, cubic CZTS into the disordered tetragonal form, 88 min after the start of the experiment, i.e., 38 min after reaching the heating plateau at 400 °C (Figure 5a, yellow line, gray background). During the isothermal period, the band at ≈330 cm^{-1} becomes incrementally sharper, and interestingly, a shoulder at around 305−310 cm^{-1} temporarily appears (Figure 5b, gray background). According to theoretical Raman spectra predictions by Ramkumar et al.,[51] this shoulder could indicate the presence of fully disordered, tetragonal CZTS (Figure 5c, gray box). This observation suggests that this phase occurs as an intermediate state during the transition from disordered cubic into disordered tetragonal CZTS. In addition, the band situated at 77 cm^{-1} increases in sharpness and intensity during the isothermal plateau (Supporting

Information, Figure S6). Using green or blue excitation lasers could provide deeper insights in future works, as the intensity of the LO modes around 360−380 cm^{-1} is significantly increased[57] compared to the red laser that was available to us.

For detailed insights, we performed a semiquantitative analysis of the Raman spectra. The bands at 77 and ≈330 cm^{-1} were fitted with Gaussian peaks, and integral band intensities and the full width at half-maximum (fwhm) were extracted. During the heating process and in the initial stage of the isothermal plateau, the fwhm of the band at ≈330 cm^{-1} decreases until it becomes constant approximately 4 h after the start of the heating process (Figure 6a). In Raman spectroscopy, the sharpness of the bands correlates -among other things like strain[58] - with the domain size: the larger the domains, the sharper the bands. Although this correlation is not as straightforward as it is for diffraction lines in XRPD, the trend in the fwhm of the ≈330 cm^{-1} band (Figure 6a, blue circles) is similar to the trend of the mean domain size observed in XRPD (b, blue circles). In the Raman spectra, we observed the appearance of the band at 77 cm^{-1}, which we associate with the beginning of the transition from disordered cubic into disordered tetragonal CZTS, around 30 min after the sample reached 400 °C (Figure 6a, magenta line). In the isothermal XRPD data, there is a steep drop in the Sn disorder ca. 30 min after the sample reached 400 °C (Figure 6b, green diamonds). During continued isothermal treatment, the intensity ratio of the Raman bands at ≈330 and at 77 cm^{-1} drops down (Figure 6a, light green squares), and the band at 77 cm^{-1} becomes sharper (green circles), which can be connected with the continued decrease in Sn disorder that was detected by XRPD (Figure 6b, green diamonds). The increasing sharpness of the band at 77 cm^{-1} could indicate that the domains with a low degree of tin ordering grow during the isothermal treatment, but it could be also partially related to the reduction of the strain due to the healing of stacking faults (Figure 6b, black squares). Isothermal, *in situ* Raman measurements at 375 °C further support these findings. After the sample reaches 375 °C, the decreasing fwhm of the ≈330 cm^{-1} band reaches a plateau (Figure 6c, blue circles) and shortly afterward the 77 cm^{-1} band, indicating that the beginning of tin ordering can be detected (magenta line). Subsequently, the intensity ratio of the bands at ≈330 and at 77 cm^{-1} drops down (light green squares), and the 77 cm^{-1} band becomes sharper. The corresponding occurrence of mean domain size growth (Figure 6d, blue circles), tin ordering (green diamonds), and fault healing (black squares) can be observed in the XRPD measurements at 375 °C on a slightly different timescale, which could be attributed to the different heating setups used (see the experimental section).

DFT and *Ab Initio* Molecular Dynamics Studies. For further supporting the experimental findings, we performed DFT and *ab initio* molecular dynamics studies. Even by using a supercomputer, there are limits in the lateral and vertical dimensions of the supercells used for these *ab initio* simulations (Supporting Information, Figure S8), which are more expensive than force field models. Unfortunately, reliable force fields for such chemically complex systems have not been developed, thus requiring *ab initio* calculations. Hence, for simulations and calculations of disordered cubic and tetragonal CZTS, we used different starting models with different sets of randomly distributed metal cations for the cation substructure (Supporting Information, Figure S9). Despite some fluctuations, they yield the same qualitative trends. Accordingly, we
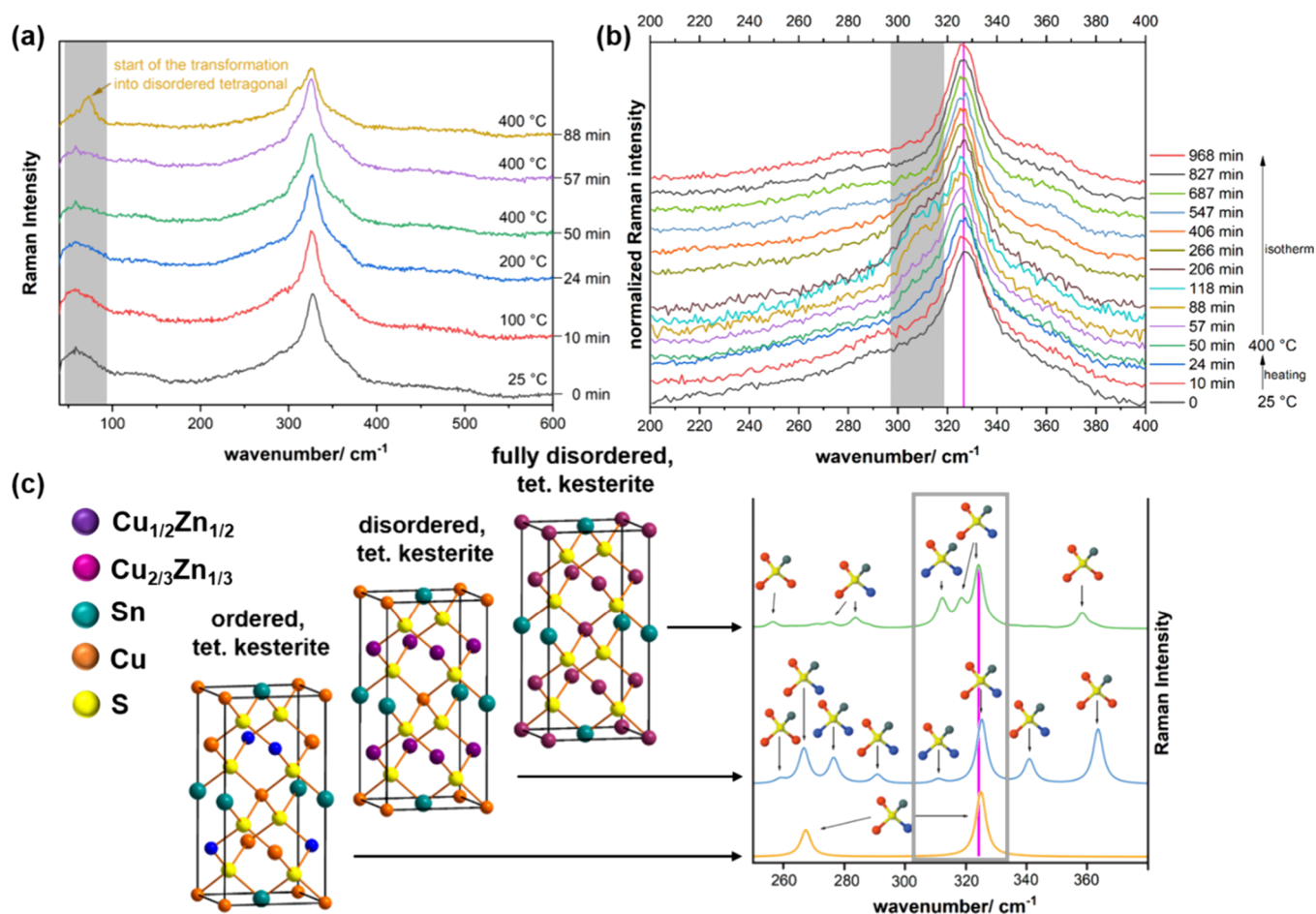
Figure 5. Temperature-dependent *in situ* Raman spectra, recorded during the isothermal heating process of disordered cubic CZTS, (a) spectra recorded during the heat-up and the initial isothermal period at 400 °C. The gray shaded area highlights the appearance of the band at 77 cm^{-1}, indicating the transformation from cubic into tetragonal kesterite; (b) excerpt of the spectra recorded during the heat-up and the isothermal period at 400 °C. The gray shaded area highlights a temporarily appearing shoulder at 305–310 cm^{-1} pointing to the intermediary appearance of fully disordered tetragonal kesterite; (c) predicted Raman spectra of ordered, disordered, and fully disordered tetragonal kesterite. Reproduced from Ramkumar et al.[51] Copyright 2022 American Physical Society (APS).

focus the data interpretation on the emerging trends rather than on the absolute values. At first, we calculated the stacking fault formation energies in cubic disordered and tetragonal disordered CZTS (Figure 7a), which indicate negative faulting energies in both disordered structures, suggesting that faulting is quite likely in these structures. In addition, we find that in the disordered, tetragonal form, stacking faults are somewhat energetically less favorable than in the cubic polymorph. Indeed, we experimentally observed that the stacking faults start to heal during heating after the tin atoms start to segregate within the cation substructure (Figure 5 and Supporting Information, Figure S4), i.e., after the beginning of the phase transition. Using the AIMD simulations, we calculated the atomic root-mean-square displacement, allowing us to obtain the diffusion coefficient. The total diffusion coefficient is computed, as well as specifically for copper and tin, both for a disordered cubic faultless (Figure 7b) and for a disordered cubic stacking faulted CZTS structure (c) at 300 (27 °C, below the transition temperature) and 750 K (477 °C, above the transition temperature). In the faultless case, the total (Figure 7b, gray bar) and the tin diffusion coefficient (magenta bar) increase moderately at higher temperatures. In the stacking faulted case instead, the total diffusion coefficient increases slightly as well, but the remarkable feature is the tin

diffusion coefficient, which spikes up much higher compared to the faultless case. This clear spike, which appears above the phase transition temperature (Supporting Information, Figure S9), suggests that the presence of stacking faults is strongly favored. As the phase transition is initiated by a segregation of tin cations, this process mechanistically requires a large mobility of tin. Hence, it is reasonable to conclude that the presence of stacking faults promotes the rearrangement of the Sn ions, leading to the phase transition process. Due to the tin segregation, the stacking faults become energetically less favorable and start to heal in a subsequent step. An experimental proof of this hypothesis would include monitoring the heating behavior of a less or more faulted sample of cubic disordered CZTS, as the sample with more faults should convert into the tetragonal polymorph more easily. However, controlling the degree of faulting during the synthesis conditions is not trivial, in particular via reactive ball milling.

■ **CONCLUSIONS**

High-energy ball milling employing WC balls and jars was proven to be a facile and easy method to synthesize pure, cubic, disordered CZTS, Cu$_2$ZnSnS$_4$. The as-milled material consists of small, intergrown and defective particles, containing a noticeable amount of stacking faults. Upon heating, the
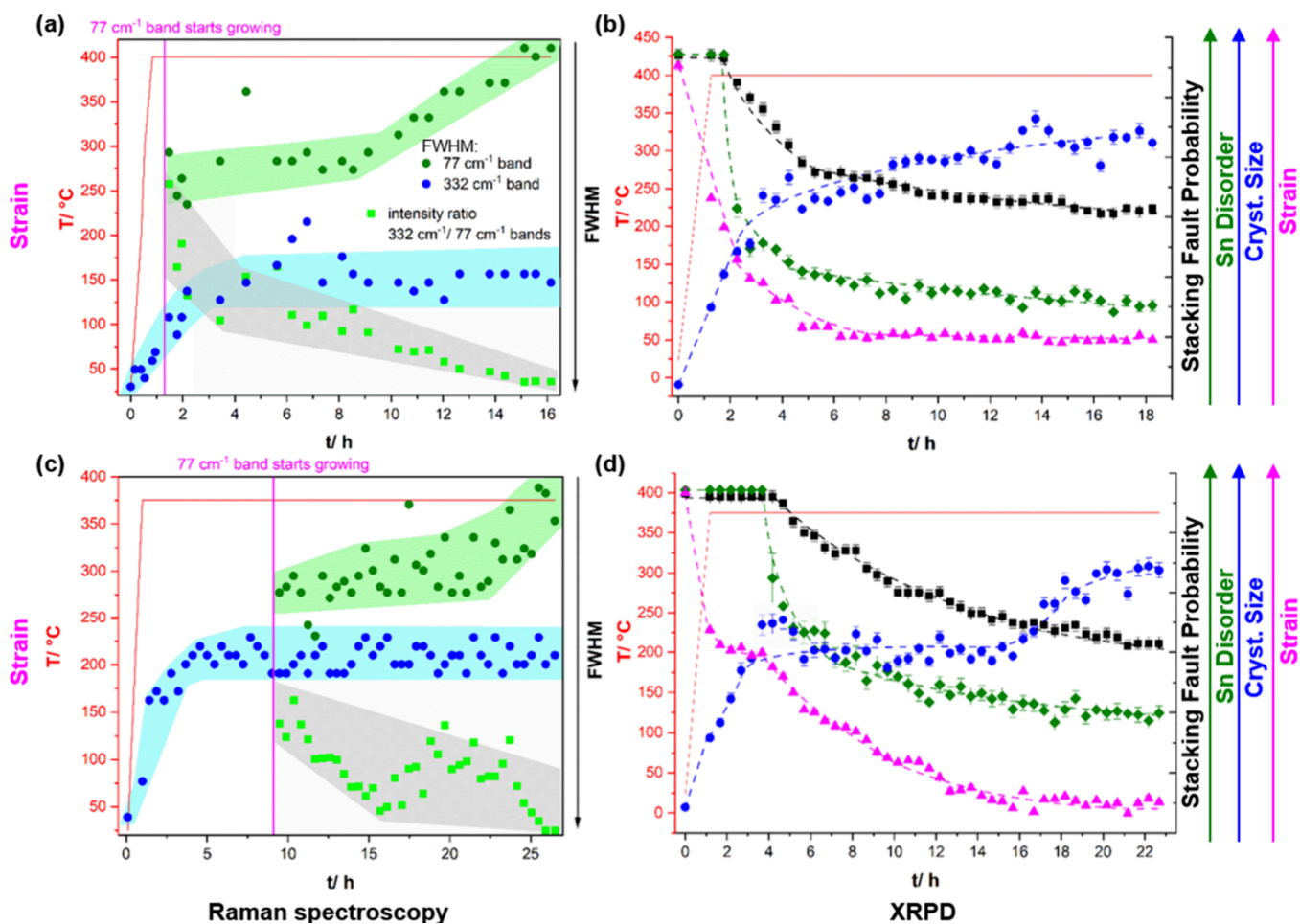
Figure 6. Results of the Raman (a,c) and XRPD (b,d) analyses of isothermal heating experiments of CZTS.
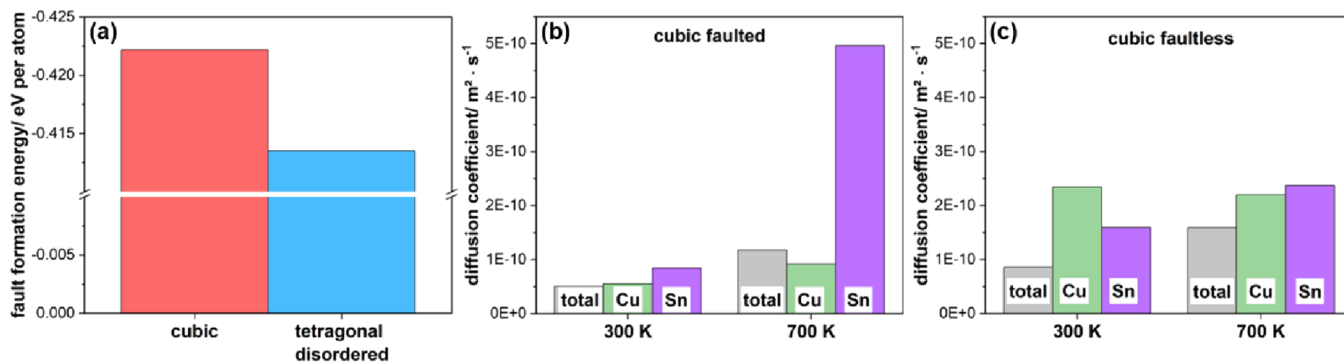

Figure 7. (a) Stacking fault formation energies derived from DFT calculations for cubic and tetragonal disordered kesterite. Diffusion coefficients derived from *ab initio* MD calculations for disordered cubic faultless (b) and disordered cubic stacking faulted (c) CZTS.

metastable, cubic, disordered CZTS slowly and irreversibly transforms into disordered, tetragonal kesterite. Temperature-dependent and isothermal *in situ* XRPD studies provided microstructural insights into this transition process. Heating induces a growth of the mean domain size, most likely by coalescence of misaligned domains. This leads to a reduction of the microstrain and to a gradual loss of the stability of the metastable, disordered cubic phase by the nanostructured state. After the domain size reaches a critical threshold, tin cations start to segregate within the occupationally disordered cation substructure, indicated by the emergence of supercell reflections, which can be indexed to the tetragonal cell in the

XRPD patterns. AIMD simulations indicate that stacking faults within the structure of cubic, disordered CZTS promote the tin diffusion and therefore potentially the tin segregation. The beginning transformation of disordered cubic CZTS into the disordered tetragonal form initiates healing of the stacking faults, which is associated with an additional microstrain reduction. DFT calculations indicate that stacking faults are energetically less favorable in the tetragonal than in the cubic disordered form of CZTS. Temperature-dependent *in situ* Raman spectroscopy qualitatively confirms the results of the XRPD studies and further indicates that, after tin segregation, copper and zinc cations remain fully occupationally disordered,

forming a "fully disordered" form of tetragonal kesterite, which has only been discussed in a theoretical study so far.[51] Upon further heating, 1/4 of the copper cations segregate, which leads to the formation of the well-known[15] disordered tetragonal kesterite. As stacking faults seem to promote the segregation of tin ions within the disordered cation substructure of disordered, cubic kesterite, further crystal engineering aiming for a stabilization of this phase should focus on the reduction of the stacking fault disorder within this material.

ASSOCIATED CONTENT

SI Supporting Information

The Supporting Information is available free of charge at https://pubs.acs.org/doi/10.1021/acs.jpcc.3c07085.

> Additional excerpts of the measured XRPD patterns, crystallographic figures and tables, and selected Rietveld plots; figures showing the results of all isothermal XRPD refinements; additional Raman data; figures showing supercells used for DFT and AIMID calculations and simulations and evolution of the mean square displacements for cubic CZTS (PDF)

AUTHOR INFORMATION

Corresponding Authors

S. Bette − Max Planck Institute for Solid State Research, Stuttgart 70569, Germany; orcid.org/0000-0003-3575-0517; Email: S.Bette@fkf.mpg.de

E. Isotta − Department of Civil, Environmental & Mechanical Engineering, University of Trento, Trento 38123, Italy; Present Address: Department of Materials Science and Engineering, Northwestern University, 2220 Campus Drive, 60208 Evanston, United States (E.I.); orcid.org/0000-0002-5864-463X; Email: eleonora.isotta@gmail.com

B. Mukherjee − Department of Civil, Environmental & Mechanical Engineering, University of Trento, Trento 38123, Italy; Present Address: Materials Research and Technology Department, Luxembourg Institute of Science and Technology (LIST), Avenue des Hauts-Fourneaux 5, L-4362 Esch/Alzette, Luxembourg (B.M.); Email: sverbinayak@gmail.com

Authors

A. Schulz − Max Planck Institute for Solid State Research, Stuttgart 70569, Germany

Z. Dallos − , Mainz 55128, Germany

U. Kolb − , Mainz 55128, Germany

Robert E. Dinnebier − Max Planck Institute for Solid State Research, Stuttgart 70569, Germany

P. Scardi − Department of Civil, Environmental & Mechanical Engineering, University of Trento, Trento 38123, Italy; orcid.org/0000-0003-1097-3917

Complete contact information is available at:
https://pubs.acs.org/10.1021/acs.jpcc.3c07085

Funding

Notes

The authors declare no competing financial interest.

REFERENCES

(1) Tanaka, T.; Nagatomo, T.; Kawasaki, D.; Nishio, M.; Guo, Q.; Wakahara, A.; Yoshida, A.; Ogawa, H. Preparation of Cu_2ZnSnS_4 thin films by hybrid sputtering. *J. Phys. Chem. Solids* **2005**, *66* (11), 1978−1981.

(2) Wallace, S. K.; Mitzi, D. B.; Walsh, A. The Steady Rise of Kesterite Solar Cells. *ACS Energy Lett.* **2017**, *2* (4), 776−779.

(3) Liu, M. L.; Huang, F. Q.; Chen, L. D.; Chen, I. W. A wide-band-gap p -type thermoelectric material based on quaternary chalcogenides of Cu_2ZnSnQ_4 (Q = S,Se). *Appl. Phys. Lett.* **2009**, *94* (20), 3−6.

(4) Yang, H.; Jauregui, L. A.; Zhang, G.; Chen, Y. P.; Wu, Y. Non-Toxic and Abundant Copper Zinc Tin Sulfide Nanocrystals for Potential High Temperature Thermoelectric Energy Harvesting. *Nano Lett.* **2012**, *12* (2), 540−545.

(5) Ortiz, B. R.; Peng, W.; Gomes, L. C.; Gorai, P.; Zhu, T.; Smiadak, D. M.; Snyder, G. J.; Stevanovic, V.; Ertekin, E.; Zevalkink, A.; et al. Ultralow thermal conductivity in diamond-like semiconductors: selective scattering of phonons from antisite defects. *Chem. Mater.* **2018**, *30* (10), 3395−3409.

(6) Jiang, Q.; Yan, H.; Lin, Y.; Shen, Y.; Yang, J.; Reece, M. J. Colossal thermoelectric enhancement in $Cu_{2+x}Zn_{1−x}SnS_4$ solid solution by local disordering of crystal lattice and multi-scale defect engineering. *J. Mater. Chem. A* **2020**, *8* (21), 10909−10916.

(7) Isotta, E.; Andrade-arvizu, J.; Syafiq, U.; Jiménez-arguijo, A.; Guc, M.; Saucedo, E.; Scardi, P. Towards Low Cost and Sustainable Thin Film Thermoelectric Devices Based on Quaternary Chalcogenides. *Adv. Funct. Mater.* **2022**, No. 2202157.

(8) Dong, Y.; Wang, H.; Nolas, G. S. Synthesis and thermoelectric properties of Cu excess $Cu_2ZnSnSe_4$. *Physica Status Solidi - Rapid Research Letters* **2014**, *8* (1), 61−64.

(9) Nagaoka, A.; Yoshino, K.; Masuda, T.; Sparks, T. D.; Scarpulla, M. A.; Nishioka, K. Environmentally friendly thermoelectric sulphide Cu_2ZnSnS_4 single crystals achieving a 1.6 dimensionless figure of meritZT. *J. Mater. Chem. A* **2021**, *9* (28), 15595−15604.

(10) Hallt, S. R.; Szymanski, J. T.; Stewart, J. M. Kesterite, $Cu_2(Zn,Fe)SnS_4$, and Stannite, $Cu_2(Zn,Fe)SnS_4$, Structurally Similar But Distinct Minerals. *Can. Mineral.* **1978**, *16* (57), 131−137.

(11) Walsh, A.; Chen, S.; Wei, S. H.; Gong, X. G. Kesterite thin-film solar cells: Advances in materials modelling of Cu_2ZnSnS_4. *Adv. Energy Mater.* **2012**, *2* (4), 400−409.

(12) Siebentritt, S.; Schorr, S. Kesterites—a challenging material for solar cells. *Prog. Photovoltaics* **2012**, *20* (6), 1114−1129.

(13) Scragg, J. J. S.; Choubrac, L.; Lafond, A.; Ericson, T.; Platzer-Björkman, C. A low-temperature order-disorder transition in Cu_2ZnSnS_4 thin films. *Appl. Phys. Lett.* **2014**, *104* (041911), 041911−041911.

(14) Rey, G.; Redinger, A.; Sendler, J.; Weiss, T. P.; Thevenin, M.; Guennou, M.; El Adib, B.; Siebentritt, S. The band gap of $Cu_2ZnSnSe_4$: Effect of order-disorder. *Appl. Phys. Lett.* **2014**, *105* (11), No. 112106.

(15) Schorr, S.; Hoebler, H.-J.; Tovar, M. A neutron diffraction study of the stannite-kesterite solid solution series. *Eur. J. Mineral.* **2007**, *19* (1), 65−73.

(16) Schorr, S.; Gonzalez-Aviles, G. -situ investigation of the structural phase transition in kesterite. *Physica Status Solidi (A) Applications and Materials Science* **2009**, *206* (5), 1054−1058.

(17) Malerba, C.; Valentini, M.; Mittiga, A. Cation Disorder in Cu_2ZnSnS_4 Thin Films: Effect on Solar Cell Performances. *Sol. RRL* **2017**, *1*, 1700101−1700101.

(18) Rudisch, K.; Ren, Y.; Platzer-Björkman, C.; Scragg, J. Order-disorder transition in B-type Cu_2ZnSnS_4 and limitations of ordering

through thermal treatments. *Appl. Phys. Lett.* **2016**, *108*, 231902–231902.

(19) Valentini, M.; Malerba, C.; Menchini, F.; Tedeschi, D.; Polimeni, A.; Capizzi, M.; Mittiga, A. Effect of the order-disorder transition on the optical properties of Cu_2ZnSnS_4. *Appl. Phys. Lett.* **2016**, *108*, 211909–211909.

(20) Chen, Z.; Sun, Q.; Zhang, F.; Mao, J.; Chen, Y.; Li, M.; Chen, Z. G.; Ang, R. Mechanical alloying boosted SnTe thermoelectrics. *Mater. Today Phys.* **2021**, *17*, 100340–100340.

(21) Isotta, E.; Fanciulli, C.; Pugno, N. M.; Scardi, P. Effect of the Order-Disorder Transition on the Seebeck Coefficient of Nano-structured Thermoelectric Cu_2ZnSnS_4. *Nanomaterials* **2019**, *9* (5), 762–762.

(22) Isotta, E.; Syafiq, U.; Ataollahi, N.; Chiappini, A.; Malerba, C.; Luong, S.; Trifiletti, V.; Fenwick, O.; Pugno, N.; Scardi, P. Thermoelectric properties of CZTS thin films: effect of Cu-Zn disorder. *Phys. Chem. Chem. Phys.* **2021**, *23*, 13148–13158.

(23) Isotta, E.; Mukherjee, B.; Fanciulli, C.; Pugno, N. M.; Scardi, P. Order–Disorder Transition in Kesterite Cu_2ZnSnS_4: Thermopower Enhancement via Electronic Band Structure Modification. *J. Phys. Chem. C* **2020**, *124* (13), 7091–7096.

(24) Mukherjee, B.; Isotta, E.; Malagutti, M. A.; Lohani, K.; Rebuffi, L.; Fanciulli, C.; Scardi, P. Thermoelectric performance in disordered $Cu_2ZnSnSe_4$ nanostructures driven by ultra-low thermal conductivity. *J. Alloys Compd.* **2023**, *933*, 167756–167756.

(25) Isotta, E.; Mukherjee, B.; Bette, S.; Dinnebier, R.; Scardi, P. Static and dynamic components of Debye–Waller coefficients in the novel cubic polymorph of low-temperature disordered Cu_2ZnSnS_4. *IUCrJ.* **2022**, *9* (2), 272.

(26) Isotta, E.; Pugno, N. M.; Scardi, P. Nanostructured kesterite (Cu_2ZnSnS_4) for applications in thermoelectric devices. *Powder Diffr.* **2019**, S42.

(27) Kapusta, K.; Drygas, M.; Janik, J. F.; Jelen, P.; Bucko, M. M.; Olejniczak, Z. From magnetic cubic pre-kesterite to semiconducting tetragonal kesterite Cu_2ZnSnS_4 nanopowders via the mechanochemi-cally assisted route. *J. Alloys Compd.* **2019**, *770*, 981–988.

(28) Isotta, E.; Mukherjee, B.; Fanciulli, C.; Ataollahi, N.; Sergueev, I.; Stankov, S.; Edla, R.; Pugno, N. M.; Scardi, P. Origin of a Simultaneous Suppression of Thermal Conductivity and Increase of Electrical Conductivity and Seebeck Coefficient in Disordered Cubic Cu_2ZnSnS_4. *Phys. Rev. Appl.* **2020**, *14* (1), 064073–064073.

(29) Mukherjee, B.; Isotta, E.; Fanciulli, C.; Ataollahi, N.; Scardi, P. Topological Anderson Insulator in Cation-Disordered Cu_2ZnSnS_4. *Nanomaterials* **2021**, *11*, 2595–2595.

(30) Lu, X.; Zhuang, Z.; Peng, Q.; Li, Y. Wurtzite Cu_2ZnSnS_4 nanocrystals: A novel quaternary semiconductor. *Chem. Commun.* **2011**, *47* (11), 3141–3143.

(31) Li, Z.; Lui, A. L. K.; Lam, K. H.; Xi, L.; Lam, Y. M. Phase-Selective Synthesis of Cu_2ZnSnS_4 Nanocrystals using Different Sulfur Precursors. *Inorg. Chem.* **2014**, *53*, 10874–10880.

(32) Mainz, R.; Singh, A.; Levcenko, S.; Klaus, M.; Genzel, C.; Ryan, K. M.; Unold, T. Phase-transition-driven growth of compound semiconductor crystals from ordered metastable nanorods. *Nat. Commun.* **2014**, *5*, 1–10.

(33) Kattan, N.; Hou, B.; Fermín, D. J.; Cherns, D. Crystal structure and defects visualization of Cu_2ZnSnS_4 nanoparticles employing transmission electron microscopy and electron diffraction. *Applied Materials Today* **2015**, *1* (1), 52–59.

(34) Kattan, N. A.; Griffiths, I. J.; Cherns, D.; Fermín, D. J. Observation of antisite domain boundaries in Cu_2ZnSnS_4 by atomic-resolution transmission electron microscopy. *Nanoscale* **2016**, *8* (30), 14369–14373.

(35) Engberg, S.; Symonowicz, J.; Schou, J.; Canulescu, S.; Jensen, K. M. Ø. Characterization of Cu_2ZnSnS_4 Particles Obtained by the Hot-Injection Method. *ACS Omega* **2020**, *5* (18), 10501–10509.

(36) Fonoll-Rubio, R.; Andrade-Arvizu, J.; Blanco-Portals, J.; Becerril-Romero, I.; Guc, M.; Saucedo, E.; Peiró, F.; Calvo-Barrio, L.; Ritzer, M.; Schnohr, C. S.; Placidi, M.; Estradé, S.; Izquierdo-Roca, V.; Pérez-Rodríguez, A. Insights into interface and bulk defects in a

high efficiency kesterite-based device. *Energy Environ. Sci.* **2021**, *14* (1), 507–523.

(37) Azanza Ricardo, C. L.; Girardi, F.; Cappelletto, E.; D'Angelo, R.; Ciancio, R.; Carlino, E.; Ricci, P. C.; Malerba, C.; Mittiga, A.; Di Maggio, R.; Scardi, P. Chloride-based route for monodisperse Cu_2ZnSnS_4 nanoparticles preparation. *J. Renewable Sustainable Energy* **2015**, *7* (4), 043150–043150.

(38) Syafiq, U.; Ataollahi, N.; Maggio, R. D.; Scardi, P. Solution-Based Synthesis and Characterization of Cu_2ZnSnS_4 (CZTS) Thin Films. *Molecules* **2019**, *24* (19), 3454–3454.

(39) Coelho, A. A. TOPAS and TOPAS-Academic: an optimization program integrating computer algebra and crystallographic objects written in C++. *J. Appl. Crystallogr.* **2018**, *51* (1), 210–218.

(40) Cheary, R. W.; Coelho, A. A fundamental parameters approach to X-ray line-profile fitting. *J. Appl. Crystallogr.* **1992**, *25* (2), 109–121.

(41) Cheary, R. W.; Coelho, A. A.; Cline, J. P. Fundamental Parameters Line Profile Fitting in Laboratory Diffractometers. *J. Res. Natl. Inst. Stand. Technol.* **2004**, *109* (1), 1–25.

(42) Pawley, G. S. Unit-cell refinement from powder diffraction scans. *J. Appl. Crystallogr.* **1981**, *14* (6), 357–361.

(43) Coelho, A. A.; Evans, J. S. O.; Lewis, J. W. Averaging the intensity of many-layered structures for accurate stacking-fault analysis using Rietveld refinement. *J. Appl. Crystallogr.* **2016**, *49* (5), 1740–1749.

(44) Bette, S.; Takayama, T.; Duppel, V.; Poulain, A.; Takagi, H.; Dinnebier, R. Ernst, Crystal structure and stacking faults in the layered honeycomb, delafossite-type materials $Ag_3LiIr_2O_6$ and $Ag_3LiRu_2O_6$. *Dalton Trans.* **2019**, *48*, 9250–9259.

(45) Bette, S.; Hinrichsen, B.; Pfister, D.; Dinnebier, R. E. A routine for the determination of the microstructure of stacking-faulted nickel cobalt aluminium hydroxide precursors for lithium nickel cobalt aluminium oxide battery materials. *J. Appl. Crystallogr.* **2020**, *53* (1), 76–87.

(46) Kresse, G.; Furthmüller, J. Efficiency of ab-initio total energy calculations for metals and semiconductors using a plane-wave basis set. *Comput. Mater. Sci.* **1996**, *6* (1), 15–50.

(47) Kresse, G.; Furthmüller, J. Efficient iterative schemes for ab initio total-energy calculations using a plane-wave basis set. *Phys. Rev. B* **1996**, *54* (16), 11169–11186.

(48) Perdew, J. P.; Burke, K.; Ernzerhof, M. Generalized gradient approximation made simple. *Phys. Rev. Lett.* **1996**, *77* (18), 3865–3868.

(49) Perdew, J. P.; Ruzsinszky, A.; Csonka, G. I.; Vydrov, O. A.; Scuseria, G. E.; Constantin, L. A.; Zhou, X.; Burke, K. Restoring the density-gradient expansion for exchange in solids and surfaces. *Phys. Rev. Lett.* **2008**, *100* (13), 1–4.

(50) Scragg, J. J. S.; Larsen, J. K.; Kumar, M.; Persson, C.; Sendler, J.; Siebentritt, S. Cu–Zn disorder and band gap fluctuations in $Cu_2ZnSn(S,Se)_4$: Theoretical and experimental investigations. *Phys. Status Solid. B* **2016**, *253* (2), 247–254.

(51) Ramkumar, S. P.; Petretto, G.; Chen, W.; Miranda, H. P. C.; Gonze, X.; Rignanese, G. M. First-principles investigation of CZTS Raman spectra. *Phys. Rev. Mater.* **2022**, *6* (3), No. 035403.

(52) Rietveld, H. M. A profile refinement method for nuclear and magnetic structures. *J. Appl. Crystallogr.* **1969**, *2* (2), 65–71.

(53) Scardi, P.; Azanza Ricardo, C. L.; Perez-Demydenko, C.; Coelho, A. A. Whole powder pattern modelling macros for TOPAS. *J. Appl. Crystallogr.* **2018**, *51* (6), 1752–1765.

(54) Scardi, P. Diffraction Line Profiles in the Rietveld Method. *Cryst. Growth Des.* **2020**, *20* (10), 6903–6916.

(55) Fernandes, P. A.; Salomé, P. M. P.; da Cunha, A. F. Study of polycrystalline Cu_2ZnSnS_4 films by Raman scattering. *J. Alloys Compd.* **2011**, *509* (28), 7600–7606.

(56) Selyshchev, O.; Havryliuk, Y.; Valakh, M. Y.; Yukhymchuk, V. O.; Raievska, O.; Stroyuk, O. L.; Dzhagan, V.; Zahn, D. R. T. Raman and X-ray Photoemission Identification of Colloidal Metal Sulfides as Potential Secondary Phases in Nanocrystalline Cu2ZnSnS4 Photo-voltaic Absorbers. *ACS Appl. Nano Mater.* **2020**, *3* (6), 5706–5717.

(57) Dimitrievska, M.; Fairbrother, A.; Fontané, X.; Jawhari, T.; Izquierdo-Roca, V.; Saucedo, E.; Pérez-Rodríguez, A. Multiwavelength excitation Raman scattering study of polycrystalline kesterite Cu2ZnSnS4 thin films. *Appl. Phys. Lett.* **2014**, *104* (2), No. 021901.

(58) Scardi, P.; Veneri, S.; Leoni, M.; Polini, R.; Traversa, E. Lattice disorder and texture in diamond coatings deposited by HFCVD on Co-cemented tungsten carbide. *Thin Solid Films* **1996**, *290−291*, 136−142.